A Numerical Study of Raindrop Impact Phenomena: The Rigid Case[1]

C. Huang, J. M. Bradford, and J. H. Cushman[2]

ABSTRACT

The Marker and Cell (MAC) numerical technique was used to examine the raindrop impact phenomenon. This experiment simulated the impact of a spherical drop on a rigid surface. Results indicated that the impact pressures were neither uniform nor constant, with extremely high values at the very instant of impact and diminishing to about five times the steady-state stagnation pressure after 5 μsec. The maximum pressure was at the contact circumference. The jetting velocity at the rigid surface was twice the impact velocity. The results implied that three critical factors important in defining resistance against raindrop impact were (i) soil deformation characteristics, (ii) soil shearing strength, and (iii) surface microrelief.

Additional Index Words: **soil erosion, Marker and Cell (MAC) technique, soil strength, soil stress.**

Huang, C., J. M. Bradford, and J. H. Cushman. 1982. A numerical study of raindrop impact phenomena: the rigid case. Soil Sci. Soc. Am. J. 46:14–19.

Soil detachment by the impact of falling raindrops is the major process contributing to interrill erosion (Young and Wiersma, 1973). A major concern of raindrop impact is not only soil detachment, but also the formation of thin-layered, low-permeability surface seals (McIntyre, 1958a; 1958b). Surface seals act as a mechanical barrier for water movement, gas exchange, and seedling growth, resulting in an adverse rooting environment (Cary and Evans, 1974). The seal enhances surface runoff and reduces subsurface water recharge.

Much research has been conducted on soil detachment under simulated rainfall (Rose, 1960; Moldenhauer and Koswara, 1968; Cruse and Larson, 1977; Al–Durrah and Bradford, 1981). Most of these studies were performed with controlled rainfall and disturbed soil media. Soil detachment from raindrop impact was related to either a raindrop parameter (e.g., momentum, kinetic energy) or a soil parameter. These studies provided relationships between raindrop impact and soil detachment but, due to their empirical nature, did not give insight into the mechanisms of the detachment process.

Materials engineers have studied the high speed liquid–solid impact erosion phenomenon on turbine blades, airplane wings, and windows (Fyall and King, 1970; 1974; Springer, 1976). Most of the engineering approaches were mechanistic in nature as opposed to the "black box" type of studies used in agricultural soil erosion. This difference in approach can be attributed to the difference in materials investigated. In high speed impact studies, the materials commonly used were aluminum, plexiglass, or rubber. They are uniform and have well-defined stress–strain relationships. Soil, on the other hand, is a three-phase system (solid, liquid, and gas), the behavior of which under stress is extremely difficult to define. A soil core prepared in the laboratory may be termed uniform in the scale of the size of the core; however, microscopically, at the scale of a raindrop (2–5 mm), the core may not be uniform at all. Despite the differences in target material and impact speed, e.g., ≥300 m/sec vs. <10 m/sec, the principles and techniques used by materials engineers to describe impact phenomena can be transferred to studies of raindrop impact on a soil surface.

If we examine the action of a falling drop striking a solid surface, two modes of action are noted. One is the compressive stress from the impact, and the other is the shearing from the lateral jetting water. Thus the questions that need answering are: (i) what

[1] Contribution from USDA–ARS in cooperation with Agron. Dep., Purdue Univ. Journal Art. no. 8486. Received 20 Apr. 1981. Approved 15 Aug. 1981.

[2] Graduate Research Assistant, Soil Scientist, USDA–ARS, and Assistant Professor, respectively, Dep. of Agronomy, Purdue University, West Lafayette, IN 47907.

is the magnitude of the impact stress, and (ii) what are the velocities of the lateral outflow? Two experimental techniques can be used to approach these questions (Fyall and King, 1970; 1974). One is the use of high speed photographic techniques to show the time series of flow patterns. Velocities are calculated from the traces of the drop boundaries. The second technique is to use electronic transducer and signal conditioning equipment to record the impact force. These two techniques provide an in-depth examination of the impact process, but the hardware limitations prevent the mechanistic delineation of the impact phenomena. Photographic techniques require shutter speeds up to 5,000 frames per second, and the transducer method records the impact force with no spatial differentiation. Both techniques require sophisticated equipment and do not give a microscopic description of the impact.

In this paper, numerical methods are used to examine the raindrop impact phenomenon. The numerical simulation represents a spherical drop of water striking a rigid surface. By solving the basic governing fluid dynamic equations, we present the time histories of stress and velocity distribution within the drop. From these results, we discuss some of the implications to the raindrop impact–soil detachment phenomenon.

BASIC EQUATIONS AND NUMERICAL TECHNIQUE

The governing equations describing the dynamic phenomena of fluids are the momentum or Navier–Stokes equation (Eq. [1]) and continuity equation (Eq. [2]). Both are expressed for fluid under inviscid, incompressible flow conditions (Daily and Harleman, 1966). The body (gravity) force is neglected because of its small magnitude. These equations become:

$$\frac{\partial \vec{V}}{\partial t} + \nabla \cdot (\vec{V}\vec{V}) = \frac{-1}{\rho}\nabla P, \text{ and} \quad [1]$$

$$\nabla \cdot \vec{V} = 0, \quad [2]$$

where, $\vec{V}$ is velocity vector, P is pressure, ρ is the density of water, t is time, $\nabla\cdot$ is divergence operator, and ∇ is gradient operator. The viscous drag by the solid surface was neglected because of the high Reynolds number (in the order of 10^4) as well as the small thickness of the boundary layer, which is <10% of the depth of the lateral flow based on the calculation of boundary layer on a flat plate (Daily and Harleman, 1966). The effects of surface tension also were not considered in this study.

The three-dimensional liquid–solid impact problem can be simplified to a two-dimensional one by assuming axisymmetry. The problem domain then is a vertical plane passing through the center of the drop. This is depicted in Fig. 1. The problem is formulated in cylindrical coordinates. Writing the velocity vector ($\vec{V}$) in terms of its vertical (V_z) and lateral (V_r) components, Eq. [1] and [2] became:

$$\frac{\partial}{\partial t}V_r + \frac{1}{r}\frac{\partial(rV_r^2)}{\partial r} + \frac{\partial(V_rV_z)}{\partial z} = \frac{-1}{\rho}\frac{\partial P}{\partial r}, \quad [3]$$

$$\frac{\partial}{\partial t}V_z + \frac{1}{r}\frac{\partial(rV_rV_z)}{\partial r} + \frac{\partial(V_z^2)}{\partial z} = \frac{-1}{\rho}\frac{\partial P}{\partial z}, \text{ and} \quad [4]$$

$$\frac{1}{r}\frac{\partial}{\partial r}(rV_r) + \frac{\partial V_z}{\partial z} = 0. \quad [5]$$

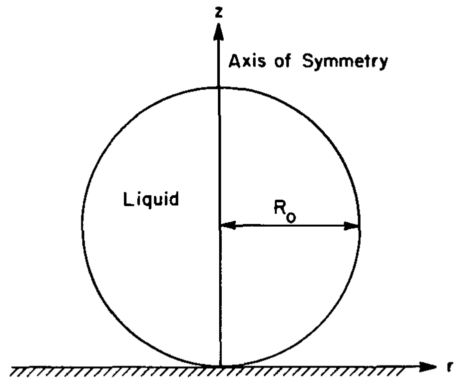

Fig. 1—The problem domain and the coordinate systems.

The initial conditions ($t = 0$) over the domain of calculations are $P = P_o$, $V_z = V_o$, and $V_r = 0$, where P_o is the ambient atmospheric pressure and V_o is the impact velocity. The required boundary conditions are:

1) along the axis of symmetry ($r = 0$):

$$V_r = 0; \quad \frac{\partial P}{\partial r} = 0$$

$$\frac{\partial V_z}{\partial r} = 0;$$

2) on the free surface:

$$P = P_o; \text{ and}$$

3) on the liquid–solid interface ($z = 0$):

$$V_z = 0.$$

The numerical technique used in this experiment is the Marker and Cell (MAC) method (Harlow and Welch, 1965). This technique was originally developed by a group of scientists at the Los Alamos Scientific Laboratory in 1965. Since then, several revisions in the solution procedures have been suggested. We used the modified MAC technique which is described in detail by Browne (1978).

The MAC technique is a finite difference scheme. The region of interest is divided into cells. Markers are placed in these cells which initially contain fluid. Initial velocities and pressures are specified in each fluid cell. The finite difference forms of the continuity and momentum equations are solved to obtain the new velocities and pressure at some small time (Δt) later. Each marker is then moved according to its velocities and the time interval (e.g., displacement = velocity × time). The problem domain is then redefined according to the new boundary, and the calculation is repeated as often as is necessary. Because this problem is solved in a fixed frame, the method is Eulerian and the equations are discretized in both space and time. This technique has the following distinctive features: (i) it utilizes the special markers to trace the fluid motion; and (ii) it solves the primary physical variables, velocity and pressure, as opposed to the conventional incompressible flow techniques at which the dependent variables are vorticity and stream function. The use of primary variables in free-surface flows makes it easy to apply the free-surface boundary conditions as well as easy to visualize the physical significance of the solution. Thus, the MAC technique is very useful in solving free-surface fluid flow problems.

The governing differential equations (Eqs. [3], [4], and [5]) were approximated in the forward–time–center–space (FTCS) difference form. The stability limitation of the FTCS difference scheme is that of Courant–Friedrichs–Lewy (CFL) criterion (Roache, 1972), which states:

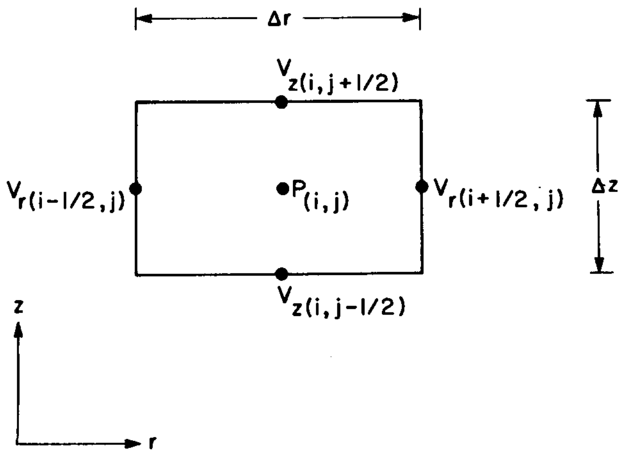

Fig. 2—Locations of velocities and pressure in a MAC cell.

$$C = V\frac{\Delta t}{\Delta r} < 1, \qquad [6]$$

where C is the Courant number, V is velocity, and Δr and Δt are space and time discretizations.

The calculation domain is discretized into cells of size $\Delta r \times \Delta z$, with cell center being designated by i in the r-direction and j in z-direction (Fig. 2). The lateral velocity (V_r) values are located at the side faces of a cell, and the vertical velocity components (V_z) at the upper and lower boundaries. The pressure (P) is designated at the center of the cell. If values are required at other points, they are obtained by simple interpolation, e.g.,

$$V_{r(i,j)} = \frac{1}{2}[V_{r(i+1/2,j)} + V_{r(i-1/2,j)}], \text{ and} \qquad [7]$$

$$(V_rV_z)_{(i+1/2,j-1/2)} = \frac{1}{4}[V_{r(i+1/2,j)} + V_{r(i+1/2,j-1)}][V_{z(i,j-1/2)} + V_{z(i+1,j-1/2)}]. \qquad [8]$$

Expressing Eq. [3] in FTCS scheme for the point ($i + \frac{1}{2}$, j), it becomes:

$$\frac{1}{\Delta t}(V^{n+1}_{r(i+1/2,j)} - V^n_{r(i+1/2,j)}) + \frac{1}{r_{(i+1/2)}\Delta r}[r_{(i+1)}(V^n_{r(i+1,j)})^2 - r_{(i)}(V^n_{r(i,j)})^2] + \frac{1}{\Delta z}[(V^n_rV^n_z)_{(i+1/2,j+1/2)} - (V^n_rV^n_z)_{(i+1/2,j-1/2)}] = \frac{-1}{\rho\Delta r}[P^{n+1}_{(i+1,j)} - P^{n+1}_{(i,j)}] \qquad [9]$$

where r_i, which is equal to $i \times \Delta r$, is the radial distance from the origin; superscript n indicates current time values; and $n + 1$, the values at interval Δt later. Rearranging terms, Eq. [9] is written as:

$$V^{n+1}_{r(i+1/2,j)} = V^n_{r(i+1/2,j)} - \frac{\Delta t}{r_{(i+1/2)}\Delta r}[r_{(i+1)}(V^n_{r(i+1,j)})^2 - r_{(i)}(V^n_{r(i,j)})^2] - \frac{\Delta t}{\Delta z}[(V^n_rV^n_z)_{(i+1/2,j+1/2)} - (V^n_rV^n_z)_{(i+1/2,j-1/2)}] + \frac{\Delta t}{\rho\Delta r}[P^{n+1}_{(i,j)} - P^{n+1}_{(i+1,j)}]. \qquad [10]$$

Likewise, Eq. [4] is expressed in finite difference form for the point (i, $j + \frac{1}{2}$) to give:

$$V^{n+1}_{z(i,j+1/2)} = V^n_{z(i,j+1/2)} - \frac{\Delta t}{r_{(i)}\Delta r}[r_{(i+1/2)}(V^n_zV^n_r)_{(i+1/2,j+1/2)} - r_{(i-1/2)}(V^n_zV^n_r)_{(i-1/2,j+1/2)}] - \frac{\Delta t}{\Delta z}[(V^n_{z(i,j+1)})^2 - (V^n_{z(i,j)})^2] + \frac{\Delta t}{\rho\Delta z}[P^{n+1}_{(i,j)} - P^{n+1}_{(i,j+1)}]. \qquad [11]$$

And the continuity equation (Eq. [5]) at (i,j) is given as:

$$D^n_{(i,j)} = \frac{1}{r_{(i)}\Delta r}[r_{(i+1/2)}V^n_{r(i+1/2,j)} - r_{(i-1/2)}V^n_{r(i-1/2,j)}] + \frac{1}{\Delta z}(V^n_{z(i,j+1/2)} - V^n_{z(i,j-1/2)}) = 0 \qquad [12]$$

A simultaneous iteration procedure on the pressure and velocity components is used to solve the finite difference equations. The iteration loop is:

1) Calculate $(D^{n+1}_{(i,j)})^m$ using Eq. [12], where m indicates the mth iteration. Note that for $m = 1$, $V^{n+1}_{r(i,j)}$ and $V^{n+1}_{z(i,j)}$ are $V^n_{r(i,j)}$ and $V^n_{z(i,j)}$.

2) Calculate $(P^{n+1}_{(i,j)})^m$ using Eq. [13] given below:

$$(P^{n+1}_{(i,j)})^{m+1} = (P^{n+1}_{(i,j)})^m - \frac{\lambda}{\rho}(D^{n+1}_{(i,j)})^m, \qquad [13]$$

where λ is a relaxation parameter, which for stability, is given by:

$$\lambda \leq \frac{1}{\Delta t[(\frac{1}{\Delta r})^2 + (\frac{1}{\Delta z})^2]}. \qquad [14]$$

Note that for $m = 1$, $P^{n+1}_{(i,j)}$ will be $P^n_{(i,j)}$.

3) Calculate $(V^{n+1}_{r(i+1/2,j)})^{m+1}$ using Eq. [10] and the latest iterative value for the P's. In the case that the calculation domain is scanned with both i and j increasing, this gives:

$$(V^{n+1}_{r(i+1/2,j)})^{m+1} = \eta^n_{(i+1/2,j)} + \frac{\Delta t}{\rho\Delta r}\left[(P^{n+1}_{(i,j)})^{m+1} - (P^{n+1}_{(i+1,j)})^m\right], \qquad [15]$$

where $\eta^n_{(i+1/2,j)}$ contains velocity values that do not change during the iteration.

4) Similarly, calculate:

$$(V^{n+1}_{r(i-1/2,j)})^{m+1} = \eta^n_{(i-1/2,j)} + \frac{\Delta t}{\rho\Delta r}\left[(P^{n+1}_{(i-1,j)})^{m+1} - (P^{n+1}_{(i,j)})^{m+1}\right], \qquad [16]$$

$$(V^{n+1}_{z(i,j+1/2)})^{m+1} = \zeta^n_{(i,j+1/2)} + \frac{\Delta t}{\rho\Delta z}\left[(P^{n+1}_{(i,j)})^{m+1} - (P^{n+1}_{(i,j+1)})^m\right], \qquad [17]$$

and

$$(V^{n+1}_{z(i,j-1/2)})^{m+1} = \zeta^n_{(i,j-1/2)} + \frac{\Delta t}{\rho\Delta z}\left[(P^{n+1}_{(i,j-1)})^{m+1} - (P^{n+1}_{(i,j)})^{m+1}\right], \qquad [18]$$

where $\zeta^n_{(i,j)}$ is defined similar to $\eta^n_{(i,j)}$.

5) $(D^{n+1}_{(i,j)})^{m+1}$ can now be calculated and the whole process repeated to convergence. Convergence here is when $\max[D^{n+1}_{(i,j)}]$ is less than some small value, typically 0.0001.

Once the convergence criterion is reached, the values at the $n + 1$ time level are assigned as "current." After moving the markers according to their new velocities and defining new liquid boundaries, the calculation is repeated for the next time step.

A FORTRAN program was implemented for the numerical calculation. The storage requirement for a calculation domain of 1,800 cells (30 radial $\times$ 60 axial) is 110k words. The computer time for each time cycle on a CDC-6500/6600 dual machine system is approximately 8 sec. The space (Δr, Δz) and time (Δt) discretizations are 0.05 and

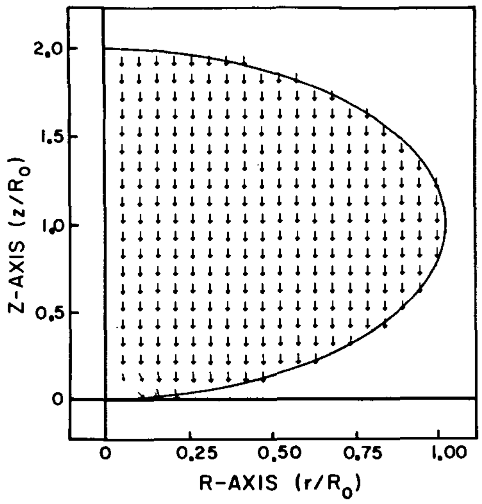

Fig. 3—The velocity distribution at nondimensional time 0.002 (real time 0.4 μsec). The scales of R and Z axes are normalized with respect to the radius of the drop (R_o). The nondimensional velocities (as referenced to the impact velocity, V_o) near the solid surface (Z = 0.025) are: 0.26, 0.52, 1.26, and 1.09, respectively.

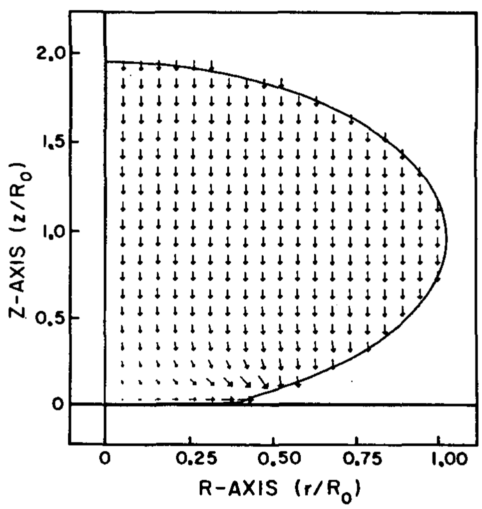

Fig. 5—The velocity distribution at nondimensional time 0.024 (real time 4.8 μsec). The nondimensional velocities near the solid surface (Z = 0.025) are: 0.13, 0.27, 0.41, 0.55, 0.74, 0.92, 1.26, and 1.59, respectively.

0.001, respectively. These values are nondimensional and are normalized in terms of their corresponding reference scales. The reference length scale is the radius of the spherical drop, R_o, and the reference time scale (t_o) is defined as R_o/V_o, where V_o is the initial impact velocity. The input parameters are: the shape and size of the drop, and the impact velocity and initial pressure field. The output of the program provides the velocities and pressure distribution within the calculation domain for different time levels. The pressure at the liquid–solid interface is the impact stress applied to the solid domain.

The results presented in this report were from the simulation of a spherical water drop falling vertically onto a rigid surface.

RESULTS AND DISCUSSION

The time history of velocity and pressure distributions within the liquid domain are shown in Fig. 3 through 9. These results were presented in nondimensional form as reference velocity V_o and reference pressure $0.5 \times \rho \times V_o^2$. The reference length ($R_o$) and time ($t_o$) scales are given in the previous section.

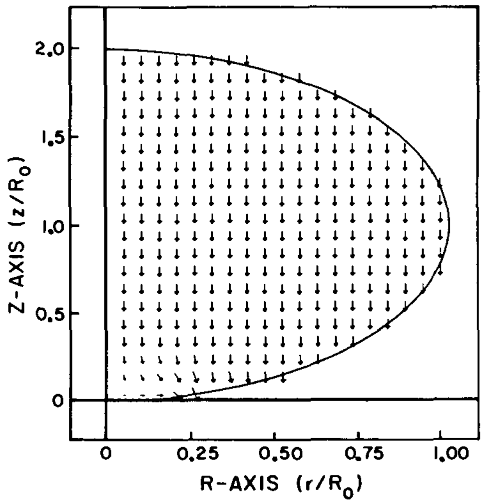

Fig. 4—The velocity distribution at nondimensional time 0.004 (real time 0.8 μsec). The nondimensional velocities near the solid surface (Z = 0.025) are: 0.19, 0.38, 0.60, 1.09, and 1.56, respectively.

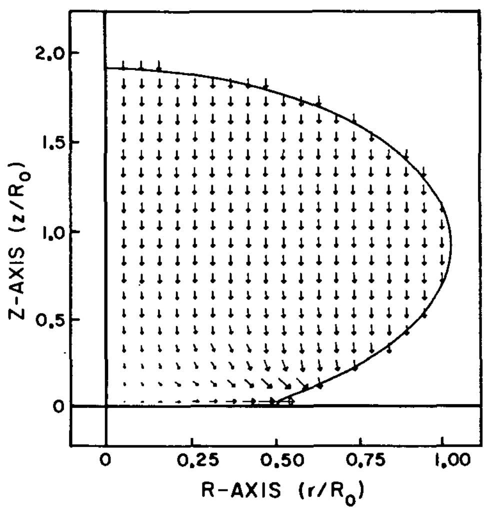

Fig. 6—The velocity distribution at nondimensional time 0.053 (real time 10.6 μsec). The nondimensional velocities near the solid surface (Z = 0.025) are: 0.11, 0.22, 0.34, 0.46, 0.60, 0.74, 1.01, 1.29, 1.68, and 2.01, respectively.

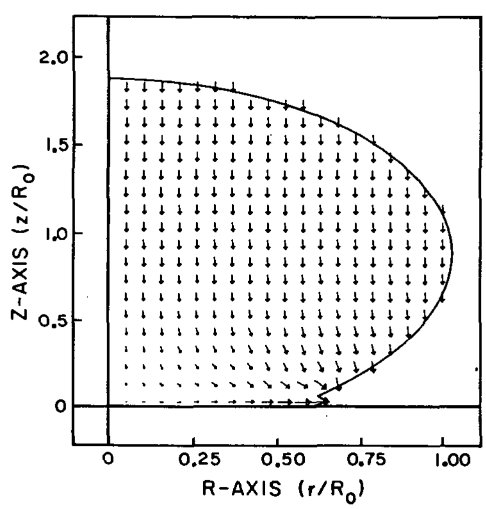

Fig. 7—The velocity distribution at nondimensional time 0.089 (real time 17.8 μsec). The nondimensional velocities near the solid surface (Z = 0.025) are: 0.08, 0.17, 0.25, 0.34, 0.42, 0.50, 0.68, 0.86, 1.15, 1.44, 1.66, and 1.88, respectively.

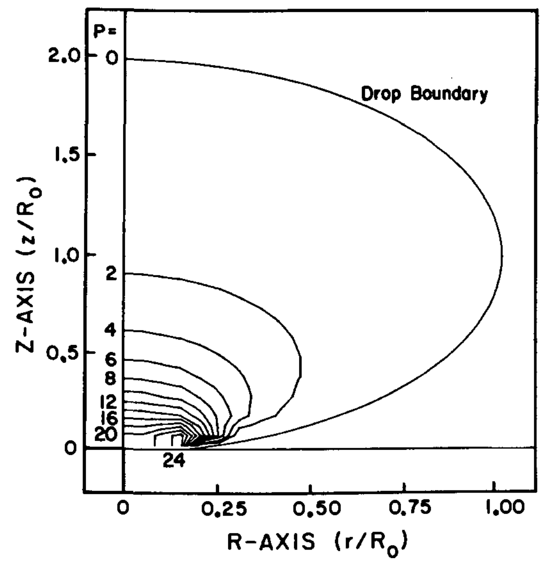

Fig. 8—The isobars within the drop at nondimensional time 0.004 (real time 0.8 μsec). The pressure is normalized with respect to the steady-state stagnation pressure (50 kPa).

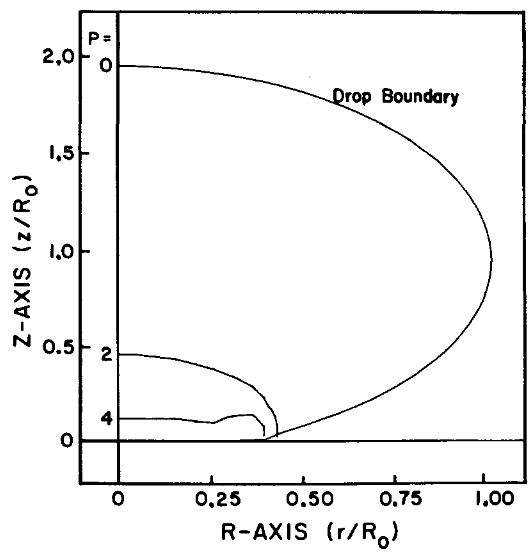

Fig. 9—The isobars within the drop at nondimensional time 0.024 (real time 4.8 μsec).

Note that we only need to know the size of the drop and the impact velocity to define all the reference scales. The reference pressure was selected because it describes the steady-state stagnation pressure under constant velocity, V_o; in other words, it is the pressure on a fixed surface normal to the stream of the flow. For a 4-mm diam (R_o = 0.002 m) drop falling at 10 m/sec (V_o), the reference time scale (t_o) is 0.2 millisec, and the reference pressure is 50 kPa. The following discussion will use this set of reference values to demonstrate a realistic setting. The pressure distribution was represented by isobars within the drop. The free boundary is an isobaric line because the pressure at the free surface is always equal to the ambient atmospheric pressure. If gauge pressure was used, as in our case, the pressure at this liquid boundary was zero. The velocity field was indicated by arrows. Each arrow represents the velocity vector at that certain location, with the arrow head pointing to the direction of the flow and the size proportional to the magnitude of the velocity. Those arrows near the top of the drop were at their initial impact velocities; thus they may be used as references when we compare the velocities near the solid surface. Also, due to symmetry, we only show one-half of a drop.

Let us examine the velocity field at t = 0.002 (Fig. 3). If translated into real-time scale, t = 0.002 corresponds to 0.4 μsec after a 4-mm diam drop travelling at 10 m/sec encountered the solid surface. We see that at t = 0.4 μsec, the fluid near the contact region was stationary. The region which was influenced by the solid surface was very limited. As time proceeded, the contact area and the region of influence propagating within the liquid domain increased (Fig. 4, 5, 6, and 7). The velocities at the contact surface were laterally dominant with their values ranging from near zero at the contact center to 1.9 times the initial impact velocity at the contact circumference (Fig. 6 and 7). About 18 μsec after the impact, a jet stream started to develop with a velocity about twice the impact velocity.

Figures 8 and 9 show the pressure distributions at two time levels; 0.8 and 4.8 μsec, respectively. Immediately after impact, within 1 μsec, extremely high pressures were calculated at the impact surface. At 0.8 μsec, the pressure ranged from 1,200 kPa (24 $\times$ reference pressure) at the contact circumference to 1,050 kPa (21 $\times$ reference pressure) at the center of the contact area. The high pressure within the liquid domain diminished quickly; at 4.8 μsec after impact, the pressures were about 200 kPa (5 $\times$ ref. pressure). The pressure gradient at the contact surface also decreased with time, but the maximum pressure still remained at the contact circumference. The sharp decrease in pressure at the initial stage of impact was demonstrated in Fig. 10, where the maximum pressure at different times was plotted. Extrapolating back to time zero, we see that the pressure approaches infinity. This infinite pressure is the result of our assumptions that the system is isothermal and water behaves as an incompressible fluid. When the stress at a point is being evaluated, this infinite pressure phenomenon is known as the singularity problem in stress analysis. Physically, the infinity is presented by the fact that the high initial pressure is absorbed in the bulk compressibility of water, giving rise to an emitted compression wave. In other words, immediately after

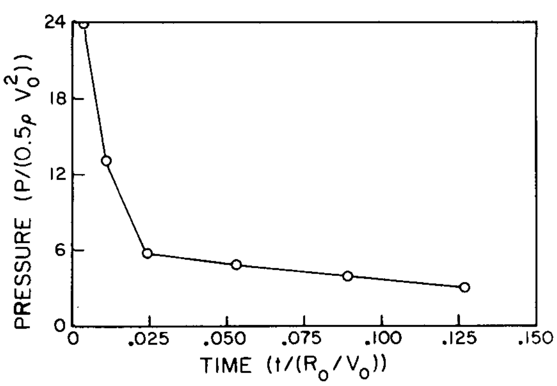

Fig. 10—The maximum pressures vs. time after impact, both in nondimensional scales.

impact, compressible fluid mechanics governs, and the impact pressure is in the magnitude of the "water hammer" pressure, which is defined as $\rho \times C_o \times V_o$, where C_o is the acoustic velocity in undisturbed water (Daily and Harleman, 1966). Taking C_o = 1,500 m/sec, we found that the water hammer pressure is 15,000 kPa, which is 300 times the reference pressure. Results from sonic speed liquid–solid impact studies suggested that the initial time period in which compressible mechanics applies is about 0.004 μsec (nondimensional time 2×10^{-5}; Springer, 1976). The incompatability in time (nanosecond vs. microsecond) and in velocity (sonic vs. $\leq$10 m/sec) justifies the usage of incompressible flow equations to simulate the rain drop impact phenomenon despite the unaccountability at the very instant of impact.

Ghadiri and Payne (1977) suggested that the stress distribution is not uniform on the raindrop–soil contact surface and that the stress may be concentrated around the periphery of the drop. The numerical example presented here showed that the impact stress varies with time and space, and the maximum stress was at the contact circumference. As we have shown, the magnitude of the impact pressure can not be predicted by the conventional steady-state stagnation pressure, at least for the initial stage of impact. The temporal variation was attributed to the curvature of the drop surface. This unsteadiness can be easily comprehended because the impact area changed from a point to some finite area with time. The nonuniform, unsteady stress distribution was also observed in high-speed (near sonic) liquid–solid impact studies (Springer, 1976).

The increased lateral jetting velocity was the result of initially high pressures. The near-doubled lateral velocity as compared to its impact velocity was in agreement with those obtained under near-sonic speed impact studies (Fyall and King, 1970; 1974). The effects of this accelerated lateral jet stream as related to soil detachment are twofold: first, this flow will exert large shearing stresses on the soil surface; and secondly, on surface irregularities, this jet stream greatly increases the soil susceptibility to tensile failure. This is shown in Fig. 11 and is believed to be the most damaging process in raindrop impact–soil detachment phenomena.

The implication of this study is that it is possible to examine a complicated physical phenomenon by numerical techniques. From this type of study, we can isolate the parameters which are critical. This example suggested that in order to define a soil resistance parameter against raindrop impact, we need to know (i) the deformation characteristics under nonuniform compressive stresses; (ii) the shear strength; and (iii) the microscale (in the range of millimeters) surface geometry. After this, we then can compile a mechanistic model which will describe the behavior of soil under raindrop impact.

In summary, we have presented numerical simulations of a spherical water drop striking a rigid surface. The impact pressures were neither uniform nor constant. Extremely high pressures occurred at the very instant of impact and diminished to about five times the steady-state stagnation pressure after 5 μsec. The maximum pressure was at the circumference of the water drop contact surface. The pressure gradient within the drop decreased very quickly. The lateral jetting velocity was twice the impact velocity. This high velocity lateral jet stream is believed to be the crucial mechanism in raindrop–soil detachment process.

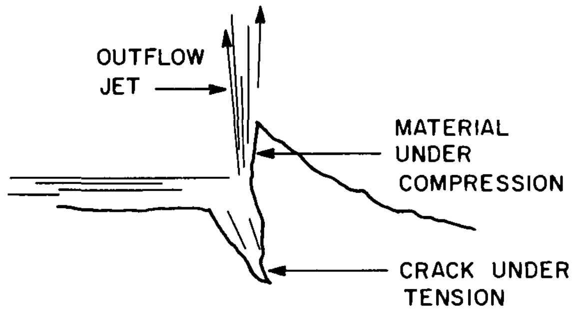

Fig. 11—The effect of lateral jetting on the surface irregularities.

ACKNOWLEDGMENT

The authors would like to thank Dr. Gilbert J. B. Hwang, Idaho National Engineering Lab., Idaho Falls, for his help in the initial setup of the numerical program.

LITERATURE CITED

1. Al-Durrah, M., and J. M. Bradford. 1981. New methods of studying soil detachment due to waterdrop impact. Soil Sci. Soc. Am. J. 45:949–953.
2. Browne, L. W. B. 1978. The marker and cell technique. p. 223–247. *In* John Noye (ed.) Numerical simulation of fluid motion. North-Holland Pub. Co., Amsterdam, Holland.
3. Cary, J. W., and D. D. Evans. 1974. Soil crust. Univ. Arizona Agric. Exp. Stn. Tech. Bull. no. 214.
4. Cruse, R. M., and W. E. Larson. 1977. Effect of soil shear strength on soil detachment due to raindrop impact. Soil Sci. Soc. Am. J. 40:777–781.
5. Daily, J. W., and D. R. F. Harleman. 1966. Fluid dynamics. Addison-Wesley Pub. Co., Reading, Massachusetts.
6. Fyall, A. A., and R. B. King. (ed.) 1970. Proc. 3rd Int. Conf. on Rain Erosion and Allied Phenomena (2 vol.) Hampshire, England, 11–13 Aug. 1970. Royal Aircraft Establishment, Farnborough, England.
7. Fyall, A. A., and R. B. King. (ed.) 1974. Proc. 4th Int. Conf. on Rain Erosion and Allied Phenomena (2 vol.) Meersburg, Germany. 8–10 May 1974. Royal Aircraft Establishment, Farnborough, England.
8. Ghadiri, H., and D. Payne. 1977. Raindrop impact stress and the break down of soil crums. J. Soil Sci. 28:247–258.
9. Harlow, F. H., and J. E. Welch. 1965. Numerical calculation of time dependent viscous incompressible flow of fluid with free surface. Phys. Fluids 8:2182–2189.
10. McIntyre, D. S. 1958a. Permeability measurement of soil crust formed by raindrop impact. Soil Sci. 85:185–189.
11. McIntyre, D. S. 1958b. Soil splash and the formation of surface crust by raindrop impact. Soil Sci. 85:261–266.
12. Moldenhauer, W. C., and J. Koswara. 1968. Effect of initial clod size on characteristics of splash and water erosion. Soil Sci. Soc. Am. Proc. 32:875–879.
13. Roache, P. J. 1972. Computational fluid dynamics. Hermosa Publishing Co., Albuquerque, New Mexico.
14. Rose, C. W. 1960. Soil detachment caused by rain fall. Soil Sci. 89:28–35.
15. Springer, G. S. 1976. Erosion by liquid impact. Halstead Press, New York.
16. Young, R. A., and J. L. Wiersma. 1973. The role of rainfall impact in soil detachment and transport. Water Resource Res. 9:1629–1636.